Inertial geometric quantum logic gates

D.Turyansky[1], O. Ovdat[2], R. Dann[3,4], Z. Aqua[2], R. Kosloff[4], B. Dayan[2], and A.Pick[1]

[1]Department of Applied Physics, The Hebrew University of Jerusalem, Jerusalem 9190401, Israel

[2]Department of Chemical Physics, Weizmann Institute of Science, Rehovot 76100, Israel

[3]Max-Planck-Institut für Quantenoptik, Hans-Kopfermann-Straße 1, D-85748 Garching, Germany

[4]The Institute of Chemistry, The Hebrew University of Jerusalem, Jerusalem 9190401, Israel

We present rapid and robust protocols for STIRAP and quantum logic gates. Our gates are based on geometric phases acquired by instantaneous eigenstates of a *slowly accelerating* "inertial" Hamiltonian. To begin, we establish the criteria for inertial evolution and subsequently engineer pulse shapes that fulfill these conditions. These tailored pulses are then used to optimize geometric logic gates. We analyze a realization of our protocols with ^{87}Rb atoms, resulting in gate fidelity that approaches the current state-of-the-art, with marked improvements in robustness.

1 Introduction

High-fidelity quantum logic gates play a critical role in advancing large-scale atom-based quantum computing systems [1–4]. Presently, the record fidelity stands at 99.99% for single-qubit gates [5, 6], 99.5% for two-qubit gates using hyperfine qubits [7, 8], and 99% for qubits combining hyperfine and Rydberg levels [9]. Advancing these capabilities remains a primary objective in quantum computation research. Gate fidelity is limited by both fundamental and technical noise sources [10]. Accordingly, protocols are optimized to reduce errors by compromising the different noise sources, e.g., minimizing population in radiative states, reducing the input power, and the gate time. Recent work on Rydberg-based gates suggests that robust pulses, designed to withstand Doppler and intensity noise, could surpass existing state-of-the-art gate fidelities. Such pulse optimization is anticipated to yield substantial enhancements in error-correcting codes [11, 12]. These developments motivated our search for general principles that produce rapid and robust gate protocols.

Our approach is a modification of traditional adiabatic following of eigenstates, where a slowly varying system adheres to an instantaneous eigenstate during its evolution [13]. While adiabatic protocols exhibit robustness against noise, their limitation lies in speed. Here, we use *inertial protocols* [14] – where the system adheres to eigenstates of an inertial Hamiltonian (defined below) – which match the robustness of adiabatic protocols but offer faster execution. We present optimal pulse shapes for stimulated rapid adiabatic passage [15] (STIRAP) and geometric logic gates [16–19] (Fig. 2). We optimize the simulated gate fidelity with quantum optimal control (QOCT) and include inertial constraints in the cost functional. The performance of our protocols is analyzed in Fig. 3, demonstrating gate fidelity close to the state-of-the-art with improved robustness. Inertial protocols could potentially improve additional adiabatic protocols, including quantum search [20], teleportation [21], quantum annealing [22], and additional entangling gate protocols [23, 24].

> **Contribution**
>
> Quantum computation errors can be mitigated by employing adiabatic protocols, involving slow manipulation of qubits. However, the inherent slowness of these protocols restricts their performance. In this study, we present an alternative approach that attains a comparable level of robustness by harnessing inertial protocols [14, 25]. Unlike adiabatic protocols, these strategies do not rely on slow manipulation but instead utilize slow acceleration to achieve robustness. To demonstrate the full power of this approach, we develop an algorithm that finds optimal protocols for universal quantum logic gates.

The paper is structured as follows. We begin by surveying the literature on adiabatic pro-

tools and quantum optimal control (Sec. 2), and continue by introducing the inertial theorem (Sec. 3). Then, we apply the theorem to find advantageous pulse shapes for STIRAP (Sec. 4). To quantify the advantage of our approach, we benchmark several STIRAP implementations in terms of their fidelity, robustness and pulse area (Sec. 5). In Sec. 6, we outline our QOCT algorithm, which includes inertial constraints. Sec. 7 presents an application of our STIRAP pulses for geometric quantum logic gates. Sec. 8 and Sec. 9 present an analysis of the dominant noise channels and a proposal for experimental realization with ^{87}Rd atoms. We conclude with a discussion of the advantages and shortcomings of the present approach (Sec. 10).

terdiabatic protocols are part of a larger class of methods called shortcut-to-adiabaticity (STA) methods [35]. In theory, STA can achieve a perfect fidelity in a short time. However, practical bounds on power and speed limit the fidelity in practice. Counter-diabatic driving was successfully applied to STIRAP in [36]. Combining counter-diabatic driving with superdiabatic basis states can produce even faster robust protocols [37, 38]. Our approach is a part of STA methods, which involve tracing eigenstates of modified Hamiltonians. We mention an early related proposal for following eigenstates of non-trivial invariant operators [39], which is similar in spirit to invariants that arise in the inertial frame.

2 Background

Many efforts have focused on improving adiabatic protocols, aiming to enhance fidelity within a specified pulse area while preserving their robustness [15]. Below, we survey some of these significant findings. A straightforward strategy involves seeking pulses that minimize diabatic errors, arising from population leakage from the instantaneous eigenstate. Diabatic errors can be expressed in terms of complex poles of the energy gap [26]. It follows that protocols that minimize diabatic errors involve parallel transport of instantaneous eigenvalues [27]. Another effective strategy involves fulfilling the adiabatic condition at each moment during the propagation by appropriately adjusting the instantaneous rate of change of control fields in proportion to the instantaneous energy gap [28, 29]. These methods have found success in applications including adiabatic state transfer [30–32].

Other methods extend beyond merely tracking the instantaneous eigenstates adiabatically. For example, some protocols rely on tracking "superdiabatic basis states," which are successive truncations of the series solution of the Schrödinger equation in powers of the adiabatic parameter [33]. Following superdiabatic states is favorable in computation since these states adhere more closely to the physical solution than adiabatic eigenstates. Another approach for improving adiabatic protocols consists of introducing "counter-diabatic" control fields that cancel diabatic errors [34]. Both superdiabatic and coun-

Adiabatic protocols can be improved with QOCT [40–42]. First, adiabatic protocols can be used as an initial guess for the optimization, which is aimed at increasing gate or state-transfer fidelity [23, 43, 44]. To find pulses that not only maximize the fidelity but are also robust, one can optimize an ensemble of protocols that samples realistic fluctuations [45]. In Ref. [12], analytic considerations were used to find robust optimized pulses. In [46], QOCT was used to search for solutions which are closest to the STA within a set of implementable pulses. Alternatively, the optimization functional can be modified to include constraints for adiabatic following. For example, one can add a constraint to maximize projection onto dark states [47]. A related idea is to minimize projection onto radiative states [48]. Another approach is to satisfy adiabatic condition locally [28, 49]. Yet another approach applies learning algorithms [50]. Specifically, we mention proposals that are closely related to our work, which use QOCT to improve STIRAP [28, 43, 46, 49], adiabatic Rydberg-based gates [23, 45], and non-adiabatic Rydberg gates [12, 44]. We developed a QOCT approach that finds protocols that adhere to inertial eigenstates. We find that inertial constraints produce efficient protocols, which achieve the same outcome as the unoptimized protocols with reduced pulse area. Before introducing our optimization approach, we survey key aspects of the inertial theorem.

3 The Inertial theorem

The inertial theorem exploits a temporal separation of variables to derive approximate solutions for a system's dynamics under rapid external driving [14]. The theorem is derived in Liouville space – the vector space of operators that transform states in the Hilbert space. The derivation begins by applying the Heisenberg equations of motion to the system operators, revealing a distinctive time-dependent operator basis in which the equations of motion exhibit variations on two distinct timescales. By defining a generalized time coordinate, the rapid dynamics can be effectively removed, subsequently unveiling new dynamical symmetries—operators whose Heisenberg representation remains time-independent. These symmetries, in turn, facilitate the construction of approximate analytical solutions. For closed systems, we introduce a simplified formulation of the theorem in Hilbert space. The derivation for open systems can be found in [14]. While our calculations account for noise, we present the Hamiltonian formulation here due to its simplicity.

Suppose $|\psi\rangle$ is a solution of the Schrödinger equation, $i\hbar\,\partial_t|\psi\rangle = H(t)|\psi\rangle$. Let us introduce the eigenvalue decomposition of the Hamiltonian:

$$H(t) = P\Lambda P^{-1}, \tag{1}$$

where P and Λ are instantaneous matrices of eigenvectors and eigenvalues of H respectively. Let us use the eigenvector matrix to define the state $|\tilde{\psi}\rangle = P|\psi\rangle$, which satisfies

$$i\hbar\frac{\partial\,|\tilde{\psi}\rangle}{\partial t} = \left(P^\dagger H P - i\hbar P^\dagger\frac{\partial P}{\partial t}\right)|\tilde{\psi}\rangle \equiv \tilde{H}|\tilde{\psi}\rangle. \tag{2}$$

[Eq. (2) is valid for any matrix P, not necessarily the eigenvector matrix.] Inertial frames are those in which $\tilde{H}$ can be written in the form

$$\tilde{H} = \Omega(t)\mathbb{M}(\chi), \tag{3}$$

where $\Omega(t)$ *may vary rapidly while χ is nearly stationary.* Introducing a rescaled time coordinate, $\tau = \int_0^t \Omega(t')dt'$, we obtain

$$i\hbar\frac{\partial|\tilde{\psi}\rangle}{\partial\tau} = \mathbb{M}(\chi)|\tilde{\psi}\rangle. \tag{4}$$

If $\mathbb{M}$ changes slowly compared to its energy gap, a system initialized in an eigenstate clings to it during the dynamics. The escape probability from

eigenstate $|\tilde{\psi}_n(t)\rangle$ with eigenenergy $\tilde{\varepsilon}_n$ is given by the inertiality parameter

$$\eta_I^{(n)} \equiv \max_{m\neq n}\left\{\frac{\langle\tilde{\psi}_m|\frac{\partial\mathbb{M}}{\partial\tau}|\tilde{\psi}_n\rangle}{(\tilde{\varepsilon}_m - \tilde{\varepsilon}_n)^2}\right\}, \tag{5}$$

where the ratio is maximized over all states $m \neq n$. In comparison, an eigenstate $|\psi_n(t)\rangle$ of the lab-frame Hamiltonian, H, with eigenenergy ε_n evolves adiabatically provided that the adiabaticity parameter is small

$$\eta_A^{(n)} \equiv \max_{m\neq n}\left\{\frac{\langle\psi_m|\frac{\partial H}{\partial t}|\psi_n\rangle}{(\varepsilon_m - \varepsilon_n)^2}\right\}. \tag{6}$$

We will see that in STIRAP, keeping the inertiality parameter small amounts to constraining the second-order temporal derivative of the control parameters (i.e., acceleration), while the adiabatic condition implies a small velocity.

4 Inertial conditions for STIRAP

Before introducing the inertial protocol, we review the essentials of STIRAP. In this protocol, population is transferred between two electronic states, $|1\rangle$ and $|3\rangle$, by driving transitions form these states into a third level $|2\rangle$. Introducing the vector $\mathbf{c} = [c_1(t), c_2(t), c_3(t)]$ for probability amplitudes of the electronic states, the system dynamics is governed by

$$i\hbar\frac{d}{dt}\mathbf{c}(t) = \frac{\hbar}{2}\begin{pmatrix} 0 & \Omega_1(t) & 0 \\ \Omega_1(t) & 2\Delta & \Omega_2(t) \\ 0 & \Omega_2(t) & 0 \end{pmatrix}\mathbf{c}(t). \tag{7}$$

Here, Ω_1 is the Rabi frequency of the field that couples $|1\rangle$ and $|2\rangle$ while Ω_2 couples $|2\rangle$ and $|3\rangle$. Each field is detuned from the driven atomic transition by $\hbar\Delta$, and we assume that the two-photon transition from $|1\rangle$ to $|3\rangle$ is resonant. This Hamiltonian has a zero-energy eigenstate $|D\rangle \equiv (\Omega_2|1\rangle - \Omega_1|3\rangle)/\Omega$, denoted "dark" because it is decoupled from the radiation field. To transition adiabatically from $|1\rangle$ to $|3\rangle$ by following the dark state, one needs to start the protocol with $\Omega_1 = 0$ and $\Omega_2 \neq 0$ (with $|D\rangle = |1\rangle$) and end with $\Omega_2 = 0$ and $\Omega_1 \neq 0$ (so that $|D\rangle = |3\rangle$).

Let us now construct an inertial STIRAP protocol. For simplicity, we present a derivation of our protocol in the limit of $\Delta = 0$, which

is optimal in some cases [15], but we deal later with $\Delta \neq 0$ which is the relevant regime for the STIRAP-based CZ gate (CZ) [51]. When $\Delta = 0$, the dynamics can be described by an effective two-level system, satisfying [32, 52]:

$$i\hbar \frac{d}{dt}\mathbf{b}(t) = \frac{\hbar}{2}\begin{pmatrix} \Omega_1(t) & \Omega_2(t) \\ \Omega_2(t) & -\Omega_1(t) \end{pmatrix}\mathbf{b}(t). \quad (8)$$

Here, $\mathbf{b}$ is the vector of probability amplitudes of two specially chosen basis states, expressed in terms of $\mathbf{c}$ (the explicit relation is given in [52]). While state transfer in the original basis [Eq. (7)] requires the initial and final conditions $c(0) = [1, 0, 0]$ and $c(t_f) = [0, 0, 1]$ respectively (where t_f denotes protocol duration), the new basis coefficients satisfy $b_1(0) = 1$ and $b_1(t_f) = b_2(t_f)$. We introduce the parameterization

$$\Omega_1 = \Omega(t)\sin[2\theta(t)] \quad \Omega_2 = \Omega(t)\cos[2\theta(t)], \quad (9)$$

with $\theta(0) = 0$ and $\theta(t_f) = \pi/2$. With this parameterization, Eq. (8) becomes

$$H = \Omega(t)\left(\cos 2\theta\, \sigma_z + \sin 2\theta\, \sigma_x\right). \quad (10)$$

Seeking an inertial solution, we transform the Hamiltonian to the eigenvector basis and find

$$\tilde{H} = \Omega(t)\left(\sigma_z - \frac{\chi}{2}\sigma_y\right) = \Omega(t)\mathbb{M}(\chi). \quad (11)$$

We define $\chi \equiv \frac{\dot{\theta}}{\Omega}$, where dot denotes a time derivative. Derivation details are shown in appendix A. When χ is small, the protocol is adiabatic. Yet, when χ varies slowly, it is inertial. An inertial protocol succeeds provided that (i) the initial state is $|1\rangle$ and the final state is $|2\rangle$; (ii) the eigenstates of $\mathbb{M}(\chi)$ and H coincide at the beginning and end of the protocol; and (iii) the matrix $\mathbb{M}(\chi)$ varies slowly compared to its energy gap. Formally, the conditions are:

$$(i) \quad \theta(0) = 0 \quad, \quad \theta(t_f) = \pi/2 \quad (12a)$$

$$(ii) \quad \dot{\theta}(0) = \dot{\theta}(t_f) = 0, \quad (12b)$$

$$(iii) \quad \eta_I = \frac{1}{4\Omega}\frac{\dot{\chi}}{4 + \chi^2} \ll 1 \quad \text{where } \chi \equiv \frac{\dot{\theta}}{\Omega} \quad (12c)$$

The protocol is also adiabatic when

$$(iv) \quad \eta_A = \frac{\chi}{4} \ll 1 \quad (13)$$

The adiabaticity and inertiality parameters, η_A and η_I respectively, were computed using Eqs. (5,6). In the next section, we compare the performance of several protocols. We find that protocols with a small ineriality parameter have a favorable asymptotic scaling of the infidelity and are robust to realistic noise channels.
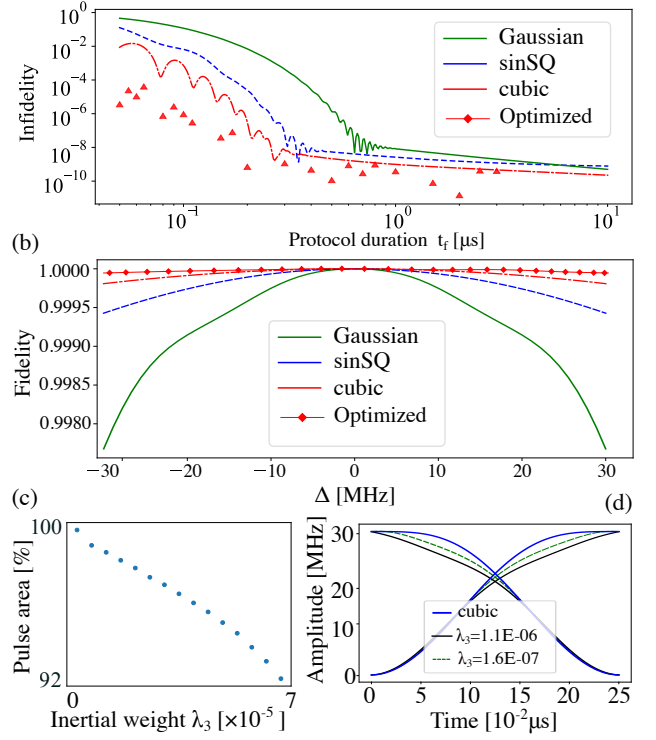

Fig. 1: (a) STIRAP infidelity versus effective pulse area ($\Omega_{\max} \cdot t_f$) for three pulse shapes [Eq. (14)]: Gaussian (green), sinSQ (blue), and cubic (red). Parameters: $\Delta = 0$MHz, $\Omega_{\max} = 50$MHz and $\gamma_{31}/2\pi = \gamma_{32}/2\pi = 3$ MHz, accounting for decay from $|3\rangle$ into $|1\rangle$ and $|2\rangle$. QOCT parameters: $\lambda_1 = 0.1, \lambda_2 = 0, \lambda_3 = 1 \cdot 10^{-7}$ (see Sec. 6). (b) Infidelity, $1 - \mathcal{F}$, versus Δ, for $t_f = 0.25\mu$s. (c) Effective pulse area, $\Omega_{\max}t_f$, (relative to cubic pulse) for protocols generated with constrained QOCT vs. weight of inertial constraint, λ_3. (d) Pulse shapes generated with QOCT with a cubic guess pulse for different values of λ_3, which achieve fidelity of 0.99.

5 Fidelity of inertial STIRAP pulses

Figure 1 compares STIRAP performance with analytic pulse shapes and with an optimized inertial pulse. The analytic functions, Ω_j (j=1,2), are Gaussian, squared sinusoidal (sinSQ) with a linear $\theta(t)$ and a sin function with a cubic $\theta(t)$:

$$\text{Gaussian}: \ \Omega_j(t) = \Omega_{\max}e^{-4(t - t_j)^2/t_f^2} \quad (14a)$$

$$\text{SinSQ}: \ \Omega_j(t) = \Omega_{\max}\sin^2[\pi(t - t_j)/2t_f] \quad (14b)$$

$$\text{Cubic}: \ \Omega_j(t) = \Omega_{\max}\sin[\theta_n(t - t_j)]. \quad (14c)$$

Here, $t_1 = t_f$ and $t_2 = 0$ while θ_n is a cubic polynomial[i]. Conditions (i) and (ii) are satisfied by the sinSQ and cubic pulses, but are violated by the Gaussian pulse. The optimized pulse is

$$^{(i)}\theta_n(t) = \sum_{n=2}^{3} C_n t^n \text{ with } C_3 = -\frac{\pi}{t_f^3}, C_2 = (\frac{\pi}{2} - C_3 t_f^3)/t_f^2.$$

found with our constrained QOCT code, which minimizes the time-averaged inertiality parameter η_I, and uses the cubic pulse as an initial guess.

To compute the infidelity, we evolve the density matrix (representing the state of the system) by solving the Lindblad master equation, with the Hamiltonian of Eq. (7) and including spontaneous emission from state $|2\rangle$. We use the open-source Python package QuTip [53]. Fidelity is defined in terms of the overlap between the target and final states, $\rho_t = |3\rangle\langle3|$ and ρ_f respectively. Formally, $\mathcal{F} \equiv 1 - \mathrm{Tr}(\sqrt{\rho_f}\rho_t\sqrt{\rho_f})^{1/2}$.

Figure 1 compares the infidelity and robustness of the protocols as a function of protocol duration t_f. In contrast to the Gaussian pulse, both the cubic and sinSQ pulses satisfy conditions (*i-ii*), and are, therefore, superior to it. The cubic pulse is better than the sinSQ pulse. This can be attributed to the fact that the energy gap between instantaneous eigenvalues is constant throughout the protocol and, hence, minimizes diabatic transitions [27]. The optimized pulse has the smallest fidelity and highest robustness. Small oscillations in the infidelity of the analytic pulses are attributed to non-adiabatic transitions that can be controlled by using mask functions that smooth the derivatives of the pulses [52].

To further substantiate the connection between inertiality and optimal adiabatic performance, we use our QOCT algorithm [Sec. 6]. We control the degree of inertiality by increasing the weight of the inertiality constraint [λ_3 in Eq. (15) below] and find that by increasing λ_3, the pulse area is reduced for a given fidelity. This is the main advantage of our optimized protocols, as it implies that they are more efficient than the analytic pulse shapes. Figure 1(c) compares pulses obtained with varying inertiality constraints in the range $\lambda_3 \in (0,7) \times 10^{-5}$. It presents the effective pulse area, $\Omega_{\max}t_f$, relative to that of the cubic protocol [Eq. (14c)], as a function of λ_3. The pulse area is reduced in the shown parameter range, as result of increasing λ_3. (We note that this trend does not hold in general. Since we are dealing with an optimization problem with multiple objective functions, it has multiple local minima. We find optimal weights for optimization by means of trial and error.) Figure 1(d) shows three representative optimized pulses, obtained with inertial weights of $\lambda_3 = 1.6 \cdot 10^{-7}$ (green dashed) and $\lambda_3 = 1.1 \cdot 10^{-6}$ (black solid).

We show also the cubic pulse shape (blue). While all shown pulses achieve STIRAP fidelity of 0.99, the smallest effective pulse area is achieved with largest λ_3. Our QOCT algorithm is explained in the following section.

6 QOCT with inertial constraints

The goal of QOCT is to find optimal pulses, Ω_1^c and Ω_2^c, and a corresponding optimal trajectory, $\rho^c(t)$, that achieve maximal fidelity given minimal input power. Here, we introduce additional constraints to find optimal solutions that are also adiabatic and inertial.[*(ii)*] Consider the functional

$$\mathcal{J}(\rho, \Omega_1, \Omega_2) = \mathrm{Tr}\{\rho_t\rho_f\} - \int_0^{t_f} dt\, \mathrm{Tr}\{\xi(\tfrac{d}{dt} - \hat{\mathcal{L}})\rho\} +$$
$$\sum_{i=1}^{2}\left\{\lambda_1 \int_0^{t_f}dt|\Omega_i|^2 + \lambda_2 \int_0^{t_f}dt|\dot{\Omega}_i|^2 + \lambda_3 \int_0^{t_f}dt|\ddot{\Omega}_i|^2\right\}$$
$$(15)$$

The first term is maximized when the final state ρ_f reaches the target state ρ_t. The second enforces solutions to satisfy the Lindblad equation, $\dot{\rho} = \hat{\mathcal{L}}\rho$, where $\hat{\mathcal{L}}$ is the Lindbladian operator and ξ is the associated Lagrange multiplier. The third is a penalty proportional to the total input power in the pulses, with the associated Lagrange multiplier λ_1. We include the last two terms to restrict the time-averaged velocity and acceleration, with Lagrange multipliers λ_2 and λ_3 respectively.

From the different methods to formulate and solve the optimization problem [54–57], we use Krotov's algorithm to find minimal solutions for $\mathcal{J}$ [58–64], which starts with guess pulses for the controls and updates them iteratively. This method has the advantage that is guarantees that the performance merits improve in each iteration [65]. Starting from initial guess pulses, Ω_1^0 and Ω_2^0, in each iteration (denoted by k), the variables ρ^k and χ^k are evolved and the pulses are updated according to an update rule, $\Omega_i^{k+1} = \Omega_i^k + \omega_i$, which guarantees that $\mathcal{J}$ decreases in each iteration. Since the pulses are generally complex, we obtain separate update rules for their real and imaginary components [$\omega_i^R(t)$ and $\omega_i^I(t)$] in each iteration. We show in appendix B that the updates satisfy the fol-

---

*(ii)*We seek inertial protocols found using inertial constraint, but add adiabatic constraints for generality.

lowing differential equations:

$$\lambda_1 \omega_i^R - \lambda_2 \frac{d^2}{dt^2}\omega_i^R + \lambda_3 \frac{d^4}{dt^4}\omega_i^R = \frac{1}{2}\text{Tr}\{\xi^k \frac{\partial \Delta\hat{\mathcal{L}}}{\partial \omega_i^R}\rho^{k+1}\}$$

$$\lambda_1 \omega_i^I - \lambda_2 \frac{d^2}{dt^2}\omega_i^I + \lambda_3 \frac{d^4}{dt^4}\omega_i^I = \frac{1}{2}\text{Tr}\{\xi^k \frac{\partial \Delta\hat{\mathcal{L}}}{\partial \omega_i^I}\rho^{k+1}\}.$$
(16)

By discretizing the time coordinate, we vectorize the functions $\omega_i^R(t)$ and $\omega_i^I(t)$ and solve Eq. (16) using linear algebra tools.

7 Geometric quantum logic gates

Robustness to noise can be achieved by cyclic adiabatic evolution (which starts and ends with the same Hamiltonian) under which a qubit's state acquires a geometric phase that depends only on the state's trajectory [66]. While non-degenerate Hamiltonians are associated with scalar (abelian) phases, degeneracy gives rise to matrix (non-abelian) phases [67]. When including both abelian and non-abelian "holonomic" operations, it is possible to realize a universal set of gates that are robust against certain types of errors [68–72]. A protocol for holonomic quantum logic gates was proposed in [18], where the qubit state acquires geometric phases by driving transitions out and back into the qubit subspace. We simulated this protocol using the pulses from Sec. 5.

Figure 2 presents numerical simulations of the gates. Single-qubit gates (panels a–b) require a tripod-level atom (insets in the bottom plots). A qubit is encoded in $|0\rangle$ and $|1\rangle$. A geometric phase gate (Pauli-Z rotation by π) is performed using two STIRAP steps to transfer population from $|1\rangle$ to the auxiliary level $|2\rangle$ and back into $|1\rangle$; The phase of one of the pulses (here Ω_2) is shifted by π in the second STIRAP step [Fig. 2(a), top] and, consequently, creates a relative phase shift of π between $|0\rangle$ and $|1\rangle$. To find favorable performance, we replace the cubic pulse with a quatric polynomial. Since our protocol contains two STIRAP steps, we search for a polynomial with zero derivative ($\theta'(t) = 0$) at the beginning, middle, and end of the protocol. Considering symmetric and antisymmetric pulses (around $t_f/2$), we find that these conditions are satisfied with a fourth order polynomial.[(iii)]

[(iii)]$\theta(t)$ is a quartic polynomial $P_4(t) = C_0 + C_2(t - \frac{t_f}{2})^2 + C_4(t - \frac{t_f}{2})^4$, with $C_0 = \frac{\pi}{2}, C_2 = -4\frac{\pi}{t_f^2}, C_4 = \frac{8\pi}{t_f^4}$.

To implement a Hadamard gate [Fig. 2(b)], one needs a third field, Ω_0. The three fields, $\Omega_{0,1,2}$, are applied following the protocol in (b1). In this case, the initial dark state is a combination of $|0\rangle$ and $|1\rangle$, whose weights are determined by the ratio of Ω_0 and Ω_1. During the protocol, a phase is acquired by the dark state, which translates into a rotation in the qubit basis [18, 19]. Finally, a CZ gate is achieved using four-level atoms with Rydberg interaction between excited states [Fig. 2(c)]. This gate operates in a regime of a weak Rydberg interaction compared to the Rabi frequencies, $V_R \ll \Omega_1, \Omega_2$. In this limit, when two atoms occupy the excited state, their interaction produces an energy shift and the wavefunction acquires a phase proportional to V_R [10]. A CZ gate is implemented by applying two STIRAP steps and tuning the time delay between the pulses so that the $|11\rangle$ component of the wavefunction acquires a π phase shift relative to other qubit states.

We simulated these protocols with the pulses from Eq. (14). For each protocol, we reconstructed the simulated gate, $\rho \to \hat{G}(\rho)$, with process tomography (reviewed in appendix C), which provides Kraus operators, G_k that expand $\hat{\mathcal{G}}$: [73]

$$\hat{\mathcal{G}}(\rho) = \sum_k G_k \rho G_k^\dagger.$$
(17)

Using this expansion, we computed the average gate fidelity, $\mathcal{F}$, defined as the overlap between the simulated and target gates ($\hat{\mathcal{G}}$ and U_0 respectively) averaged over all possible initial states. For an initial pure state, $|\psi\rangle$, the average gate fidelity $\mathcal{F}$ is given by [45, 74–76]:

$$\mathcal{F} \equiv \int_{S^{2n-1}} dV \, \langle\psi|U_0^\dagger \hat{G}(|\psi\rangle\langle\psi|)U_0|\psi\rangle =$$

$$\frac{1}{n(n+1)}\sum_k \left(\text{Tr}(M_k M_k^\dagger) + |\text{Tr}(M_k)|^2\right), \quad (18)$$

where n is the dimension of the Hilbert space ($n = 2$ or 4 for single- or two-qubit gates) and $M_k \equiv U_0^\dagger G_k$. The results are shown in Fig. 2. We plot the infidelity as a function of maximum Rabi frequency. In the CZ gate, t_f is set by requiring that the conditional phase shift is π. The quartic protocol approaches $\mathcal{F} = 1$ at the fastest rate, as expected based on Fig. 1. Unfortunately, the gate fidelity is much smaller than the STIRAP fidelity. The reason is that gate fidelities are limited by
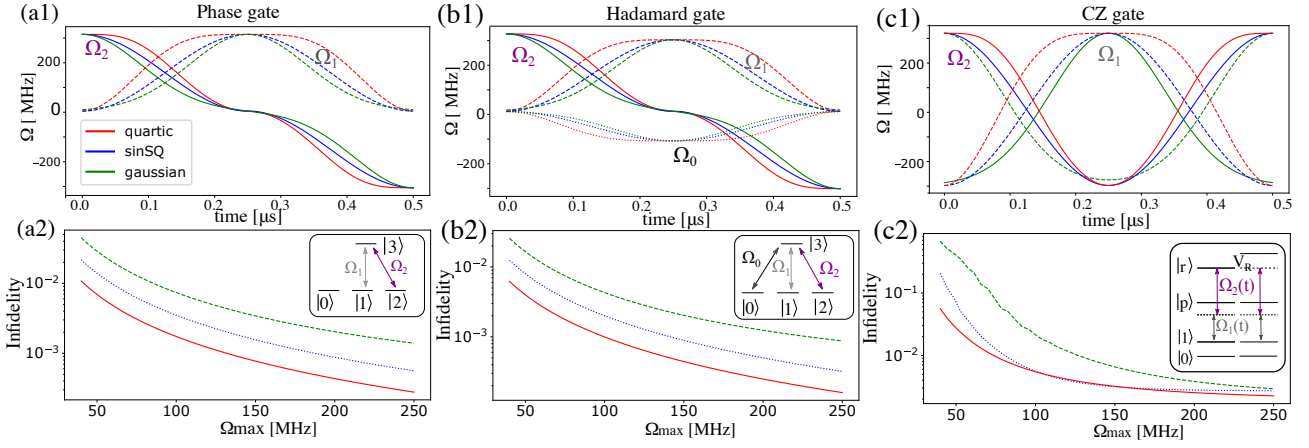
Fig. 2: **Inertial geometric gates** (a1,a2) Single-qubit phase gate, using a tripod-level atom (inset) with control pulses $\Omega_1(t)$ and $\Omega_2(t)$ that transfer population from $|1\rangle$ to $|2\rangle$ and back to $|1\rangle$, while flipping the phase of Ω_2 in the middle of the protocol [17, 18]. (a1) Gaussian (Green), sinSQ (blue) and quartic (red) pulses are shown. (a2) Gate infidelity versus Ω_{max} for the Gaussian, sinSQ, and quartic pulses. (b1-b2) Hadamard gate, using Ω_0, Ω_1 and Ω_2 and gate infidelity. (c1-c2) CZ gate, using 4-level atoms with Rydberg-induced phase shifts (inset). Pulse shapes and gate infidelity versus Ω_{max} are shown. Parameters of single-qubit gates: $\gamma/2\pi = 6\text{MHz}$, $\Delta = 0$. Phase gate: $\Omega_1^{\mathsf{max}} = \Omega_2^{\mathsf{max}} = 2\pi \times 50\text{MHz}$. Hadamard gate: $\Omega_1^{\mathsf{max}} = 2\pi \times 50\text{MHz}$, $\Omega_2^{\mathsf{max}} = (1-\sqrt{2})\Omega_1^{\mathsf{max}}$, $(\Omega_0^{\mathsf{max}})^2 = (\Omega_1^{\mathsf{max}})^2 + (\Omega_2^{\mathsf{max}})^2$. Two-qubit CZ gate: $\Omega_{\mathsf{max}}/2\pi = \Delta = 50\text{MHz}$, $V_R = 14\text{MHz}$, $\gamma_p/2\pi = 6\text{MHz}$, $\gamma_r/2\pi = 1\text{kHz}$, $\gamma_{\mathsf{dep}}/2\pi = 10\text{kHz}$.

phase errors, which are larger than population errors that limit STIRAP[iv].

8 Noise analysis

Next, we analyze the effect of noise on the CZ gate, with the pulses from Fig. 2(c). We consider qubits encoded in hyperfine states of ^{87}Rb atoms, trapped in optical tweezers. Following the noise analysis from Ref. [24, 77], we include the following imperfections: Doppler shifts, errors due to nonuniformity of Gaussian control beams, fluctuations in the amplitude and phase of the control fields, deviations in atom separation, dephasing and finite lifetimes of the electronic states. Details about our noise model (which follows Ref. [24]) are given in appendix D.

The results are shown in Fig. 3 and in Table 1. Evidently, the quartic protocol is highly robust to deviations in the detuning (Doppler shifts). When varying the detuning by 20%, the fidelity of the quartic protocol varies by 0.08% while that of the Gaussian pulse varies by $\sim 0.7\%$. In addition, the quartic pulse is highly robust to variations in intensity and decay rate of the interme-

diate STIRAP level, $|p\rangle$. We assume, for simplicity, that the control fields are co-propagating to avoid fluctuations in the two-photon detuning.[v]

However, being based on the non-blockaded Rydberg regime ($V_R < \Omega_1, \Omega_2$), this protocol is sensitive to dephasing of the Rydberg state and to fluctuations in atom separation. The latter modify the strength of atomic interaction and, consequently, the phase acquired by the $|11\rangle$ component of the wavefucntion. This drawback is a property of a non-blockaded gate, and not of the quartic or Gaussian pulse shapes that implement it. An application of inertial conditions to optimize adiabatic protocols which operate in the blockaded regime (as in [78]) are expected to

---

[iv]It is a consequence of first-order perturbation theory that population errors scale quadratically with the small parameter while phase errors scale linearly.

[v]Counter-propagating beams were treated in [15, 24]).

be highly robust and efficient.

Pulse	Quartic		Gaussian	
noise	$\mathcal{F}_{\min}$	$\mathcal{F}_{\max}$	$\mathcal{F}_{\min}$	$\mathcal{F}_{\max}$
detuning $\Delta \pm 20\%$	-0.09%	$+0.084\%$	-0.839%	0.64%
intensity $\Omega \pm 20\%$	-0.19%	$+0.11\%$	-1.68%	0.8%
lifetime $\gamma_p \pm 20\%$	-0.017%	$+0.013\%$	-0.13%	$+0.13\%$
lifetime $\gamma_r \pm 20\%$	-0.025%	$+0.028\%$	-0.025%	$+0.025\%$
dephasing $\gamma_d \pm 20\%$	-0.95%	$+0.64\%$	-0.59%	$+0.60\%$
position $\Delta x \pm 2\%$	-5.2%	0.79%	-6.71%	$+0.86\%$

Table 1: Robustness of quartic and Gaussian pulses for the CZ gate. When using parameters: $\Omega_{\max} = \Delta = 100 \times 2\pi$MHz, $t_f = 0.5\mu$s, $V_R = C_6/r^6$, with $C_6 = 14$THz/μm, $r = 10~\mu$m, $\gamma_p = 6$MHz, $\gamma_r = 1$kHz, $\gamma_d = 10$kHz, the quartic pulse fidelity is $\mathcal{F} = 0.963$ while the Gaussian pulse achieves $\mathcal{F} = 0.948$. The table shows by what percentage the fidelity changes upon changing the model parameters under realistic noise sources.
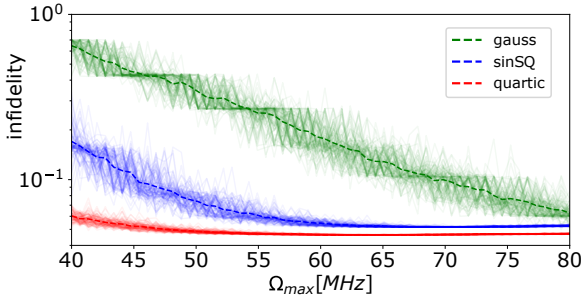

Fig. 3: Infidelity of the CZ gate protocol [Fig. 2(c)] performed with Gaussian, sinSQ, and quartic pulses, for 100 realizations of noisy model parameters. The detuning, maximum Rabi frequency, and deviation in atomic positions along and perpendicular to the tweezers' direction are Gaussian random variables, with average values listed in Table 1 and standard deviations: $\sigma_\Delta = 14$kHz, $\sigma_\Omega = 2.5$MHz, $\sigma_{dz} = 0.2\mu$m and $\sigma_{dx} = \sigma_{dy} = 0.07\mu$m respectively [6, 24]. Realization are shown by a thin lines and their average is shown by the thick dashed lines.

9   Experimental realization

Inertial protocols for population transfer in two-level systems were validated in recent work [25]. Here, We analyze a realization of our inertial protocol for quantum logic gates. We use ^{87}Rb atoms, with two possible choices of energy levels and transitions from the D2 line, as shown in Fig. 4(a-b). In particular, we are interested in analyzing realistic imperfections, including polarization and leakage errors (following the analysis from [79–82]). For example, consider a single-qubit phase gate implemented using the levels shown in Fig. 4(a). Ideally, to drive STIRAP transitions from the state $|0_L\rangle$ to $|A\rangle$ and back, we want to apply only two beams: The pulse Ω_1 with σ_+ polarization, which drives $|F = 1, m_F = -1\rangle \leftrightarrow |F' = 0, m_F = 0\rangle$, and the pulse Ω_2 with σ_- polarization, which drives $|F = 1, m_F = 1\rangle \leftrightarrow |F' = 0, m_F = 0\rangle$. However, polarization errors in the second pulse, Ω_2, produce a σ_+ component that drives the first transition, and errors in the first pulse drive the second transition. This process reduces the success probability of the protocol. To combat this issue, one can apply a DC magnetic field to shift the energy levels and tune the frequencies of the control fields to be in resonance with the shifted levels. By off-setting the frequencies of the Ω_1 and Ω_2 pulses, the error fields become off resonant and their effect is suppressed. Our calculation assumes that the magnetic field is in the weak Zeeman regime. A more accurate treatment should include nonlinear (Paschen-Back) corrections for fields exceeding 10G $^{(vi)}$. Our simulations demonstrate that the fidelity approaches unity when increasing the magnetic field [Fig. 4(c)]. Further improvement can be gained by introducing a resonant optical cavity to enhance desired transitions, e.g., using the setup of [82]. Finally, we mention that at high Rabi frequencies, coupling between the desired Rydberg level and additional levels can cause leakage and dephasing. This effect can be treated following [83, 84] but is beyond the scope of the present analysis.

10   Conclusion

In this work, we presented optimal adiabatic and inertial protocols for STIRAP and geometric single- and two-qubit gates. In inertial protocols, the system adheres to an instantaneous eigenstate of the inertial Hamiltonian, obtained from the original one by a basis change. Since inertial protocols are not required to be adiabatic in the original basis, they provide a way to

---

$^{(vi)}$Field stength of 10G corresponds to the green curve at Rabi frequency $\Omega = 50$MHz.

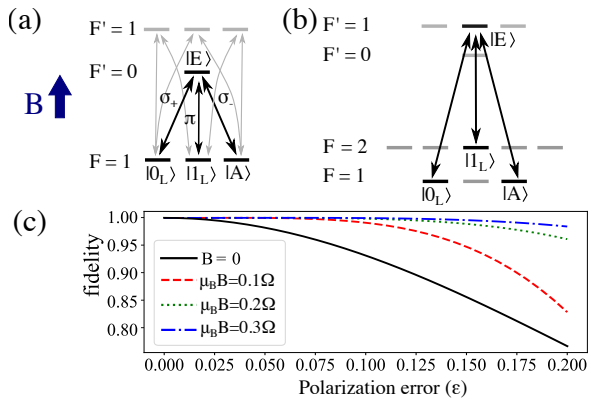Fig. 4: **Realization with Rb atoms.** (a,b) Two possible realizations of a tripod level system using the D2 line of ^{87}Rb. Desired transitions (solid lines) are shown with the corresponding polarizations: circular ($\sigma_{\pm}$) and π. Additional transitions are shown by grey arrows. (c) Infidelity of the phase gate [Fig. 3(a)] versus polarization error, ε, defined as the fraction of undesired polarization in each STIRAP pulse. Nonlinear (Paschen-Back) corrections are not included in our model (see text).

construct fast high-fidelity operations. To assess their performance, we computed the fidelity and robustness of our protocols under various perturbations, including fluctuations in atomic positions and velocities, inhomogeniety and classical noise in the control fields, polarization impurity, spontaneous emission, dephasing, and populating leakage. We found optimal inertial pulses with QOCT, extended to include adiabatic and inertial constraints, and presented several optimal pulses. Our algorithm can be further improved by searching for solutions that maximize the overlap between the dynamical and instantaneous inertial eigenstates, generalizing Ref. [47]. Although we find clear advantages to inertial geometric gates, some limitations of our approach should be mentioned. The condition that initial and final eigenstates of the inertial and original Hamiltonians must coincide [Eq. (12b)] limits our method. Without it, inertial protocols could potentially achieve high fidelities very rapidly. However, for STIRAP, this condition implies that the adiabaticity parameter must vanish at the start and end of the protocol; Consequently, our inertial STIRAP protocols are also adiabatic. To design inertial protocols that are not adiabatic, one should find quantum algorithms that do not start and end in eigenstates of the lab-frame Hamiltonian. We also mention some limitations of the geometric protocols that were im-

plemented [17, 18, 51]. First, our CZ gate is sensitive to errors in the time spent in the doubly excited Rydberg state. Secondly, two-qubit gates that use Rydberg interactions in the dispersive regime are sensitive to fluctuations in atomic positions. Application of constrained QOCT to protocols that use Rydberg blockade is expected to find pulses which are robust to such fluctuations [24]. Generally, inertial pulses are likely to improve many adiabatic protocols, including topological adiabatic algorithms [85, 86].

In light of the long list of existing "improved adiabatic protocols," our work adds simple analytic pulse shapes that yield nearly optimal solutions by satisfying the condition of small acceleration [14]. Our optimization algorithm, which uses the Lindblad formulation for the dynamics, finds efficient solutions (with reduced power requirement) that correctly balance the different noise channels with their respective branching ratios. Given the immense progress in pulse-shaping techniques for optimal control [3, 87, 88], our protocols are feasible and useful for improving the performance merits of quantum logic gates with atomic qubits.

Acknowledgement

References

[1] T.D. Ladd, F. Jelezko, R. Laflamme, Y. Nakamura, C. Monroe, J.L. O'Brien, Quantum computers. Nature **464**(7285), 45–53 (2010)

[2] M. Saffman, Quantum computing with atomic qubits and rydberg interactions: progress and challenges. Journal of Physics

B: Atomic, Molecular and Optical Physics **49**(20), 202,001 (2016)

[3] L. Henriet, L. Beguin, A. Signoles, T. Lahaye, A. Browaeys, G.O. Reymond, C. Jurczak, Quantum computing with neutral atoms. Quantum **4**, 327 (2020)

[4] M. Morgado, S. Whitlock, Quantum simulation and computing with rydberg-interacting qubits. AVS Quantum Science **3**(2), 023,501 (2021)

[5] C. Sheng, X. He, P. Xu, R. Guo, K. Wang, Z. Xiong, M. Liu, J. Wang, M. Zhan, High-fidelity single-qubit gates on neutral atoms in a two-dimensional magic-intensity optical dipole trap array. Physical Review Letters **121**(24), 240,501 (2018)

[6] H. Levine, D. Bluvstein, A. Keesling, T.T. Wang, S. Ebadi, G. Semeghini, A. Omran, M. Greiner, V. Vuletić, M.D. Lukin, Dispersive optical systems for scalable raman driving of hyperfine qubits. Physical Review A **105**(3), 032,618 (2022)

[7] H. Levine, A. Keesling, G. Semeghini, A. Omran, T.T. Wang, S. Ebadi, H. Bernien, M. Greiner, V. Vuletić, H. Pichler, et al., Parallel implementation of high-fidelity multiqubit gates with neutral atoms. Physical Review Letters **123**(17), 170,503 (2019)

[8] S.J. Evered, D. Bluvstein, M. Kalinowski, S. Ebadi, T. Manovitz, H. Zhou, S.H. Li, A.A. Geim, T.T. Wang, N. Maskara, et al., High-fidelity parallel entangling gates on a neutral atom quantum computer. arXiv preprint arXiv:2304.05420 (2023)

[9] I.S. Madjarov, J.P. Covey, A.L. Shaw, J. Choi, A. Kale, A. Cooper, H. Pichler, V. Schkolnik, J.R. Williams, M. Endres, High-fidelity entanglement and detection of alkaline-earth rydberg atoms. Nature Physics **16**(8), 857–861 (2020)

[10] M. Saffman, T.G. Walker, K. Mølmer, Quantum information with rydberg atoms. Reviews of Modern Physics **82**(3), 2313 (2010)

[11] Y. Wu, S. Kolkowitz, S. Puri, J.D. Thompson, Erasure conversion for fault-tolerant quantum computing in alkaline earth rydberg atom arrays. Nature Communications **13**(1), 4657 (2022)

[12] S. Jandura, J.D. Thompson, G. Pupillo, Optimizing rydberg gates for logical-qubit performance. PRX Quantum **4**(2), 020,336 (2023)

[13] M. Born, V. Fock, Beweis des adiabatensatzes. Zeitschrift für Physik **51**(3-4), 165–180 (1928)

[14] R. Dann, R. Kosloff, Inertial theorem: Overcoming the quantum adiabatic limit. Physical Review Research **3**(1), 013,064 (2021)

[15] N.V. Vitanov, A.A. Rangelov, B.W. Shore, K. Bergmann, Stimulated raman adiabatic passage in physics, chemistry, and beyond. Reviews of Modern Physics **89**(1), 015,006 (2017)

[16] R. Unanyan, B. Shore, K. Bergmann, Laser-driven population transfer in four-level atoms: Consequences of non-abelian geometrical adiabatic phase factors. Physical Review A **59**(4), 2910 (1999)

[17] L.M. Duan, J.I. Cirac, P. Zoller, Geometric manipulation of trapped ions for quantum computation. Science **292**(5522), 1695–1697 (2001)

[18] D. Møller, L.B. Madsen, K. Mølmer, Geometric phase gates based on stimulated raman adiabatic passage in tripod systems. Physical Review A **75**(6), 062,302 (2007)

[19] K. Toyoda, K. Uchida, A. Noguchi, S. Haze, S. Urabe, Realization of holonomic single-qubit operations. Physical Review A **87**(5), 052,307 (2013)

[20] D. Daems, S. Guerin, Analog grover search by adiabatic passage in a cavity-laser-atom system. Physical Review A **78**(2), 022,330 (2008)

[21] D. Bacon, S.T. Flammia, Adiabatic gate teleportation. Physical Review Letters **103**(12), 120,504 (2009)

[22] D. Sels, A. Polkovnikov, Minimizing irreversible losses in quantum systems by local counterdiabatic driving. Proceedings of the National Academy of Sciences **114**(20), E3909–E3916 (2017)

[23] M. Saffman, I. Beterov, A. Dalal, E. Páez, B. Sanders, Symmetric rydberg controlled-z gates with adiabatic pulses. Physical Review A **101**(6), 062,309 (2020)

[24] X. Li, X. Shao, W. Li, Single temporal-pulse-modulated parameterized controlled-phase gate for rydberg atoms. Physical Review Applied **18**(4), 044,042 (2022)

[25] C.K. Hu, R. Dann, J.M. Cui, Y.F. Huang, C.F. Li, G.C. Guo, A.C. Santos, R. Kosloff, Experimental verification of the inertial theorem control protocols. New Journal of Physics **23**(9), 093,048 (2021)

[26] J.P. Davis, P. Pechukas, Nonadiabatic transitions induced by a time-dependent hamiltonian in the semiclassical/adiabatic limit: The two-state case. The Journal of Chemical Physics **64**(8), 3129–3137 (1976)

[27] S. Guérin, S. Thomas, H. Jauslin, Optimization of population transfer by adiabatic passage. Physical Review A **65**(2), 023,409 (2002)

[28] V.S. Malinovsky, D.J. Tannor, Simple and robust extension of the stimulated raman adiabatic passage technique to n-level systems. Physical Review A **56**(6), 4929 (1997)

[29] J. Roland, N.J. Cerf, Quantum search by local adiabatic evolution. Physical Review A **65**(4), 042,308 (2002)

[30] X. Lacour, S. Guerin, H.R. Jauslin, Optimized adiabatic passage with dephasing. Physical Review A **78**(3), 033,417 (2008)

[31] G. Dridi, S. Guerin, V. Hakobyan, H.R. Jauslin, H. Eleuch, Ultrafast stimulated raman parallel adiabatic passage by shaped pulses. Physical Review A **80**(4), 043,408 (2009)

[32] G. Vasilev, A. Kuhn, N. Vitanov, Optimum pulse shapes for stimulated raman adiabatic passage. Physical Review A **80**(1), 013,417 (2009)

[33] R. Lim, M. Berry, Superadiabatic tracking of quantum evolution. Journal of Physics A: Mathematical and General **24**(14), 3255 (1991)

[34] M.V. Berry, Transitionless quantum driving. Journal of Physics A: Mathematical and Theoretical **42**(36), 365,303 (2009)

[35] D. Guéry-Odelin, A. Ruschhaupt, A. Kiely, E. Torrontegui, S. Martínez-Garaot, J.G. Muga, Shortcuts to adiabaticity: Concepts, methods, and applications. Reviews of Modern Physics **91**(4), 045,001 (2019)

[36] Y.X. Du, Z.T. Liang, Y.C. Li, X.X. Yue, Q.X. Lv, W. Huang, X. Chen, H. Yan, S.L. Zhu, Experimental realization of stimulated raman shortcut-to-adiabatic passage with cold atoms. Nature communications **7**(1), 12,479 (2016)

[37] A. Benseny, K. Mølmer, Adiabatic theorem revisited: The unexpectedly good performance of adiabatic passage. Physical Review A **103**(6), 062,215 (2021)

[38] A. Baksic, H. Ribeiro, A.A. Clerk, Speeding up adiabatic quantum state transfer by using dressed states. Physical review letters **116**(23), 230,503 (2016)

[39] X. Chen, J. Muga, Engineering of fast population transfer in three-level systems. Physical Review A **86**(3), 033,405 (2012)

[40] J. Werschnik, E. Gross, Quantum optimal control theory. Journal of Physics B: Atomic, Molecular and Optical Physics **40**(18), R175 (2007)

[41] S.J. Glaser, U. Boscain, T. Calarco, C.P. Koch, W. Köckenberger, R. Kosloff, I. Kuprov, B. Luy, S. Schirmer, T. Schulte-Herbrüggen, et al., Training schrödinger's cat: Quantum optimal control: Strategic report on current status, visions and goals for research in europe. The European Physical Journal D **69**, 1–24 (2015)

[42] C.P. Koch, U. Boscain, T. Calarco, G. Dirr, S. Filipp, S.J. Glaser, R. Kosloff, S. Montangero, T. Schulte-Herbrüggen, D. Sugny, et al., Quantum optimal control in quantum technologies. strategic report on current status, visions and goals for research in europe. EPJ Quantum Technology **9**(1), 19 (2022)

[43] N. Wang, H. Rabitz, Optimal control of population transfer in an optically dense medium. The Journal of chemical physics **104**(4), 1173–1178 (1996)

[44] Z. Fu, P. Xu, Y. Sun, Y.Y. Liu, X.D. He, X. Li, M. Liu, R.B. Li, J. Wang, L. Liu, et al., High-fidelity entanglement of neutral atoms via a rydberg-mediated single-modulated-pulse controlled-phase gate. Physical Review A **105**(4), 042,430 (2022)

[45] M.H. Goerz, E.J. Halperin, J.M. Aytac, C.P. Koch, K.B. Whaley, Robustness of high-fidelity rydberg gates with single-site addressability. Physical Review A **90**(3), 032,329 (2014)

[46] H.L. Mortensen, J.J.W. Sørensen, K. Mølmer, J.F. Sherson, Fast state transfer in a λ-system: a shortcut-to-adiabaticity approach to robust and resource optimized

control. New Journal of Physics **20**(2), 025,009 (2018)

[47] C. Brif, M.D. Grace, M. Sarovar, K.C. Young, Exploring adiabatic quantum trajectories via optimal control. New Journal of Physics **16**(6), 065,013 (2014)

[48] J.P. Palao, R. Kosloff, C.P. Koch, Protecting coherence in optimal control theory: State-dependent constraint approach. Physical Review A **77**(6), 063,412 (2008)

[49] I.R. Solá, V.S. Malinovsky, D.J. Tannor, Optimal pulse sequences for population transfer in multilevel systems. Physical Review A **60**(4), 3081 (1999)

[50] X. Yang, R. Liu, J. Li, X. Peng, Optimizing adiabatic quantum pathways via a learning algorithm. Physical Review A **102**(1), 012,614 (2020)

[51] D.B. Rao, K. Mølmer, Robust rydberg-interaction gates with adiabatic passage. Physical Review A **89**(3), 030,301 (2014)

[52] T.A. Laine, S. Stenholm, Adiabatic processes in three-level systems. Physical Review A **53**(4), 2501 (1996)

[53] J.R. Johansson, P.D. Nation, F. Nori, Qutip: An open-source python framework for the dynamics of open quantum systems. Computer Physics Communications **183**(8), 1760–1772 (2012)

[54] N. Khaneja, T. Reiss, C. Kehlet, T. Schulte-Herbrüggen, S.J. Glaser, Optimal control of coupled spin dynamics: design of nmr pulse sequences by gradient ascent algorithms. Journal of Magnetic Resonance **172**(2), 296–305 (2005)

[55] N. Rach, M.M. Müller, T. Calarco, S. Montangero, Dressing the chopped-random-basis optimization: A bandwidth-limited access to the trap-free landscape. Physical Review A **92**(6), 062,343 (2015)

[56] T. Caneva, T. Calarco, S. Montangero, Chopped random-basis quantum optimization. Physical Review A **84**(2), 022,326 (2011)

[57] M.M. Müller, R.S. Said, F. Jelezko, T. Calarco, S. Montangero, One decade of quantum optimal control in the chopped random basis. Reports on Progress in Physics **85**(7), 076,001 (2022)

[58] V.F. Krotov, I. Feldman, An iterative method for solving optimal-control problems. Engineering Cybernetics **21**(2), 123–130 (1983)

[59] V.F. Krotov, A technique of global bounds in optimal control theory. Control and Cybernetics **17**(3), 2–3 (1988)

[60] V. Krotov, in *Modeling and Control of Systems: in Engineering, Quantum Mechanics, Economics and Biosciences Proceedings of the Bellman Continuum Workshop 1988, June 13–14, Sophia Antipolis, France* (Springer, 1989), pp. 267–298

[61] D.J. Tannor, V. Kazakov, V. Orlov, Control of photochemical branching: Novel procedures for finding optimal pulses and global upper bounds. Time-dependent Quantum Molecular Dynamics pp. 347–360 (1992)

[62] V. Krotov, *Global methods in optimal control theory*, vol. 195 (CRC Press, 1995)

[63] A. Bartana, R. Kosloff, D.J. Tannor, Laser cooling of internal degrees of freedom. ii. The Journal of Chemical Physics **106**(4), 1435–1448 (1997)

[64] A. Konnov, V.F. Krotov, On global methods of successive improvement of controlled processes. Automation and Remote Control **60**(10), 1427–1436 (1999)

[65] D.M. Reich, M. Ndong, C.P. Koch, Monotonically convergent optimization in quantum control using krotov's method. The Journal of Chemical Physics **136**(10) (2012)

[66] T. Kato, On the adiabatic theorem of quantum mechanics. Journal of the Physical Society of Japan **5**(6), 435–439 (1950)

[67] P. Zanardi, M. Rasetti, Holonomic quantum computation. Physics Letters A **264**(2-3), 94–99 (1999)

[68] M. Saffman, K. Mølmer, Efficient multiparticle entanglement via asymmetric rydberg blockade. Physical Review Letters **102**(24), 240,502 (2009)

[69] D.B. Rao, K. Mølmer, Dark entangled steady states of interacting rydberg atoms. Physical Review Letters **111**(3), 033,606 (2013)

[70] D.B. Rao, K. Mølmer, Deterministic entanglement of rydberg ensembles by engineered dissipation. Physical Review A **90**(6), 062,319 (2014)

[71] D. Petrosyan, F. Motzoi, M. Saffman, K. Mølmer, High-fidelity rydberg quantum

gate via a two-atom dark state. Physical Review A **96**(4), 042,306 (2017)

[72] M. Khazali, K. Mølmer, Fast multiqubit gates by adiabatic evolution in interacting excited-state manifolds of rydberg atoms and superconducting circuits. Physical Review X **10**(2), 021,054 (2020)

[73] M.A. Nielsen, I. Chuang. Quantum computation and quantum information (2002)

[74] M.A. Nielsen, A simple formula for the average gate fidelity of a quantum dynamical operation. Physics Letters A **303**(4), 249–252 (2002)

[75] I. Beterov, M. Saffman, E. Yakshina, D. Tretyakov, V. Entin, G. Hamzina, I. Ryabtsev, Simulated quantum process tomography of quantum gates with rydberg superatoms. Journal of Physics B: Atomic, Molecular and Optical Physics **49**(11), 114,007 (2016)

[76] L.H. Pedersen, N.M. Møller, K. Mølmer, Fidelity of quantum operations. Physics Letters A **367**(1-2), 47–51 (2007)

[77] M. Saffman, T. Walker, Analysis of a quantum logic device based on dipole-dipole interactions of optically trapped rydberg atoms. Physical Review A **72**(2), 022,347 (2005)

[78] Y.C. Li, X. Chen, Shortcut to adiabatic population transfer in quantum three-level systems: effective two-level problems and feasible counterdiabatic driving. Physical Review A **94**(6), 063,411 (2016)

[79] I. Shomroni, S. Rosenblum, Y. Lovsky, O. Bechler, G. Guendelman, B. Dayan, All-optical routing of single photons by a one-atom switch controlled by a single photon. Science **345**(6199), 903–906 (2014)

[80] S. Rosenblum, O. Bechler, I. Shomroni, Y. Lovsky, G. Guendelman, B. Dayan, Extraction of a single photon from an optical pulse. Nature Photonics **10**(1), 19–22 (2016)

[81] S. Rosenblum, A. Borne, B. Dayan, Analysis of deterministic swapping of photonic and atomic states through single-photon raman interaction. Physical Review A **95**(3), 033,814 (2017)

[82] O. Bechler, A. Borne, S. Rosenblum, G. Guendelman, O.E. Mor, M. Netser, T. Ohana, Z. Aqua, N. Drucker, R. Finkelstein, et al., A passive photon–atom qubit

swap operation. Nature Physics **14**(10), 996–1000 (2018)

[83] T.G. Walker, M. Saffman, Consequences of zeeman degeneracy for the van der waals blockade between rydberg atoms. Physical Review A **77**(3), 032,723 (2008)

[84] N. Šibalić, J.D. Pritchard, C.S. Adams, K.J. Weatherill, Arc: An open-source library for calculating properties of alkali rydberg atoms. Computer Physics Communications **220**, 319–331 (2017)

[85] A. Kitaev, C. Laumann, Topological phases and quantum computation. Exact methods in low-dimensional statistical physics and quantum computing pp. 101–125 (2010)

[86] V. Lahtinen, J. Pachos, A short introduction to topological quantum computation. SciPost Physics **3**(3), 021 (2017)

[87] D. Barredo, S. De Léséleuc, V. Lienhard, T. Lahaye, A. Browaeys, An atom-by-atom assembler of defect-free arbitrary two-dimensional atomic arrays. Science **354**(6315), 1021–1023 (2016)

[88] H. Bernien, S. Schwartz, A. Keesling, H. Levine, A. Omran, H. Pichler, S. Choi, A.S. Zibrov, M. Endres, M. Greiner, et al., Probing many-body dynamics on a 51-atom quantum simulator. Nature **551**(7682), 579–584 (2017)

Supplementary Information

A Inertial STIRAP Hamiltonian

In this section, we derive Eq. (11) from the main text. We choose the parameterization

$$\Omega_1 = \Omega \sin\theta \quad , \quad \Omega_2 = \Omega \cos\theta. \tag{A1}$$

The 2-level Hamiltonian [Eq. (10) from the main text] becomes

$$H = \tfrac{\Omega^2}{2\Delta} \left(\cos 2\theta \sigma_z + \sin 2\theta \sigma_x\right) \tag{A2}$$

where σ_x and σ_z are Pauli matrices. We obtain an explicit expression for the inertial-frame Hamiltonian defined as

$$\tilde{H} \equiv P^\dagger H P - i\hbar P^\dagger \frac{\partial P}{\partial t} \tag{A3}$$

The eigenvalues are $\pm\Omega$. The eigenvector matrix is

$$P = \begin{pmatrix} \frac{\cot 2\theta + \csc 2\theta}{\sqrt{\cot\theta^2 + 1}} & \frac{\cot 2\theta - \csc 2\theta}{\sqrt{\tan\theta^2 + 1}} \\ \frac{1}{\sqrt{\cot\theta^2 + 1}} & \frac{1}{\sqrt{\tan\theta^2 + 1}} \end{pmatrix}. \tag{A4}$$

For $0 < \theta < \pi$, we find

$$P^\dagger \frac{dP}{d\theta} = \tfrac{\dot{\theta}}{2} \begin{pmatrix} 0 & -1 \\ 1 & 0 \end{pmatrix}.$$

This completes the proof of Eq. (11) in the main text.

One finds a striking similarity between the inertial-frame Hamiltonian [Eq. (11)] and the Hamiltonian one obtains when adding counter-diabatic terms to the lab-frame Hamiltonian realizing the shortcut-to-adiabaticity protocol (see Eqs. (4-5) in the Methods section of [36]). The similarity is expected, since the inner product of the instantaneous eigenvectors and their derivatives appear in both formulations. However, there is a conceptual difference which is important to point out. In shortcut-to-adiabaticity, one constructs a Hamiltonian, which may be challenging to realize, but whose eigenstates are exact solutions to the dynamics. In contrast, in our approach, the lab-frame Hamiltonian is straightforward, and the instantaneous eigenstates of the inertial-frame solutions are only approximations to the true dynamics.

B Adiabatic and inertial constraints in QOCT

In this section, we generalize Krotov's QOCT algorithm to include inertial and adiabatic constrains. Let us consider the following functional to be minimized:

$$\mathcal{J} = \mathrm{Tr}\{\rho_t \rho_f\} - \int_0^{t_f} dt \, \mathrm{Tr}\{\xi(t) \left[\tfrac{d}{dt} - \hat{\mathcal{L}}\right] \rho(t)\}$$

$$+\lambda_1 \int_0^{t_f} dt |\Omega(t)|^2 + \lambda_2 \int_0^{t_f} dt |\dot{\Omega}(t)|^2 + \lambda_3 \int_0^{t_f} dt |\ddot{\Omega}(t)|^2 \tag{B1}$$

where the two last terms correspond to the integrated velocity and acceleration. Using integration by parts, one can rewrite the first line of Eq. (B1) as:

$$\mathrm{Tr}\left\{ \rho_t \rho_f - (\xi\,\rho)\big|_0^{t_f} + \int_0^{t_f} dt \left[\rho \tfrac{d\xi}{dt} + \xi \hat{\mathcal{L}}\rho\right] \right\}. \tag{B2}$$

Krotov's algorithm starts with an initial guess from the control fields, evolves ρ and ξ and finds an updated control pulse that decreases $\mathcal{J}$. By iteratively updating the control pulse, convergence is

reached. Let us compute the change in $\mathcal{J}$ between iteration k and $k+1$ in terms of the change in ρ. Using the definitions

$$\Delta\mathcal{J} = \mathcal{J}^{(k+1)} - \mathcal{J}^{(k)} \quad , \quad \Delta\rho = \rho^{(k+1)} - \rho^{(k)}, \tag{B3}$$

we obtain:

$$\Delta\mathcal{J} = \text{Tr}\left\{\rho_t\Delta\rho - \xi^k\,\Delta\rho]\big|_0^{t_f}\right\} +$$

$$\text{Tr}\left\{\int_0^{t_f}dt\left[\Delta\rho\frac{d\xi}{dt} + \xi^k\hat{\mathcal{L}}\Delta\rho + \xi^k\Delta\hat{\mathcal{L}}\rho^{(k+1)}\right]\right\} +$$

$$-\int_0^{t_f}\left\{2\lambda_1\text{Re}[\varepsilon^k\Delta\varepsilon^*] + \lambda_1[\Delta\varepsilon_R^2 + \Delta\varepsilon_I^2]\right\} +$$

$$-\int_0^{t_f}\left\{2\lambda_2\text{Re}[\dot\varepsilon^k\Delta\dot\varepsilon^*] + \lambda_2[\Delta\dot\varepsilon_R^2 + \Delta\dot\varepsilon_I^2]\right\} +$$

$$-\int_0^{t_f}\left\{2\lambda_3\text{Re}[\ddot\varepsilon^k\Delta\ddot\varepsilon^*] + \lambda_3[\Delta\ddot\varepsilon_R^2 + \Delta\ddot\varepsilon_I^2]\right\}. \tag{B4}$$

The first 4 terms do not depend on the field increment and produce the dynamical equations for ρ and ξ. The additional terms produce the differential: $\Delta\mathcal{J}_1 + \Delta\mathcal{J}_2 + \Delta\mathcal{J}_3 + \Delta\mathcal{J}_4$ where

$$\Delta\mathcal{J}_1 = \text{Tr}\left\{\int_0^{t_f}dt\xi^k\Delta\hat{\mathcal{L}}\rho^{(k+1)}\right\}$$

$$\Delta\mathcal{J}_2 = -2\text{Re}\left[\int_0^{t_f}\lambda_1\varepsilon^k\Delta\varepsilon^* + \lambda_2\dot\varepsilon^k\Delta\dot\varepsilon^* + \lambda_3\ddot\varepsilon^k\Delta\ddot\varepsilon^*\right]$$

$$\Delta\mathcal{J}_3 = -\int_0^{t_f}\lambda_1\Delta\varepsilon_R^2 + \lambda_2\Delta\dot\varepsilon_R^2 + \lambda_3\Delta\ddot\varepsilon_R^2$$

$$\Delta\mathcal{J}_4 = -\int_0^{t_f}\lambda_1\Delta\varepsilon_I^2 + \lambda_2\Delta\dot\varepsilon_I^2 + \lambda_3\Delta\ddot\varepsilon_I^2. \tag{B5}$$

The term $\Delta\mathcal{J}_2$ vanishes on average since the integrand is rapidly oscillating. The complete differential of the third term is

$$d(\Delta\mathcal{J}_3) = \int_0^{t_f}df(\Delta\varepsilon_R, \Delta\dot\varepsilon_R, \Delta\ddot\varepsilon_R)dt =$$

$$\int_0^{t_f}\left[\frac{df}{d\Delta\varepsilon_R}\Delta\varepsilon_R + \frac{df}{d\Delta\dot\varepsilon_R}\Delta\dot\varepsilon_R + \frac{df}{d\Delta\ddot\varepsilon_R}\Delta\ddot\varepsilon_R\right]dt$$

$$\int_0^{t_f}\left[\frac{\partial f}{\partial\Delta\varepsilon_R} - \frac{d}{dt}\frac{\partial f}{\partial\Delta\dot\varepsilon_R} + \frac{d^2}{dt^2}\frac{\partial f}{\partial\Delta\ddot\varepsilon_R}\right]\Delta\varepsilon_R\,dt + \text{surface terms}$$

$$2\int_0^{t_f}(-\lambda_1\Delta\varepsilon_R + \lambda_2\Delta\ddot\varepsilon_R - \lambda_3\Delta\ddddot\varepsilon_R) + \text{surface terms} \tag{B6}$$

The surface terms vanish since the field update at the start and end point is zero, $\Delta\varepsilon_R(0) = \Delta\varepsilon_R(t_f) = 0$. Using this result (and repeating the same procedure for $\Delta\mathcal{J}_4$), we find update equations:

$$-\lambda_1\Delta\varepsilon_R + \lambda_2\Delta\ddot\varepsilon_R - \lambda_3\Delta\ddddot\varepsilon_R = \tfrac{1}{2}\text{Tr}[\xi^k\frac{\partial\Delta\hat{\mathcal{L}}}{\partial\Delta\varepsilon_R}\rho^{k+1}] \equiv F(t)$$

$$-\lambda_1\Delta\varepsilon_I + \lambda_2\Delta\ddot\varepsilon_I - \lambda_3\Delta\ddddot\varepsilon_I = \tfrac{1}{2}\text{Tr}[\xi^k\frac{\partial\Delta\hat{\mathcal{L}}}{\partial\Delta\varepsilon_I}\rho^{k+1}] \equiv G(t) \tag{B7}$$

These equations are easily solved by discretizing time and rewriting the equation in matrix form (the second-order time derivatives becomes the tridiagonal Hessian matrix and the fourth-order time derivatives is a 5-diagonal matrix). We obtain equations of the form

$$\mathbb{M}_1\Delta\varepsilon_R = \mathbb{F}$$

$$\mathbb{M}_2\Delta\varepsilon_I = \mathbb{G} \tag{B8}$$

The update rules for the control fields are found by inverting $\mathbb{M}_1$ and $\mathbb{M}_2$.
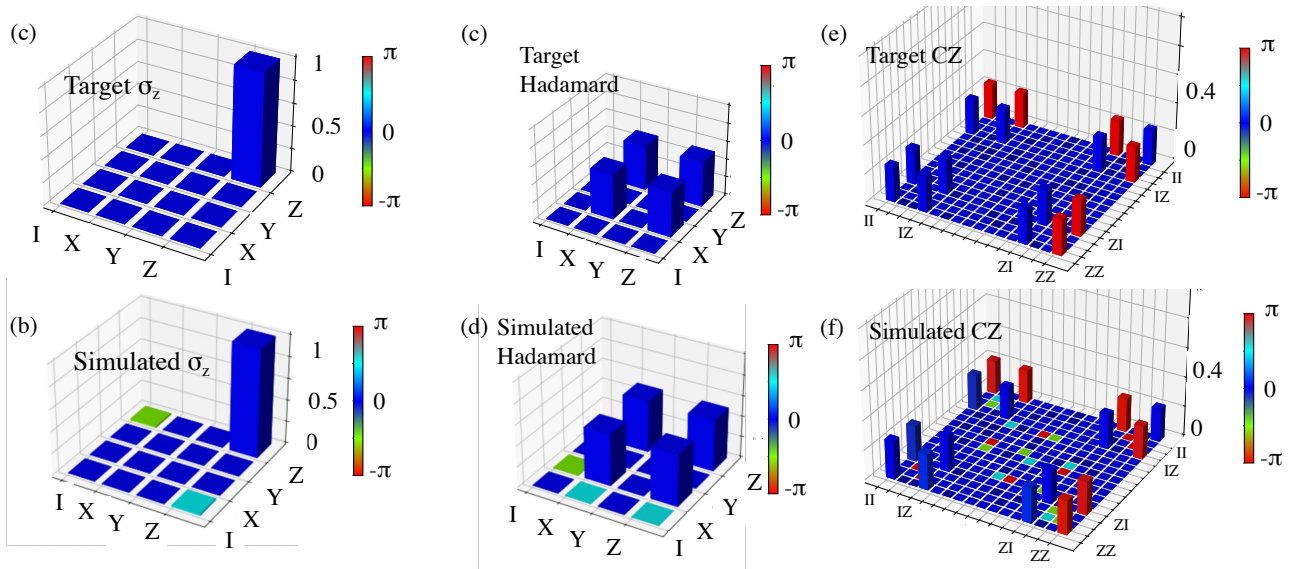
Fig. 5: **Quantum gate tomography:** Visualization of target (top) and simulated (bottom) single- and two-qubit gates. The plots show the matrix χ, which expresses the expansion coefficients of the gate transformations in terms of Pauli basis operators, $\tilde{E}_i$ [Eq. (C2)] for single-qubit gates and Kronecker products of $\tilde{E}_i$ for two-qubit gates respectively. (a–d) The matrix χ, calculated using Eq. (C4), for Hadamard and Pauli-Z single-qubit gates. (e,f) The matrix χ, calculated via Eq. (C6) for a two-qubit CZ gate.

C Quantum gate tomography

Quantum process tomography (QPT) is a method by which a quantum gate is reconstructed from simulated data (experimental or numerical). In this work, we use QPT to quantify the overlap between our simulated and target gates. In this appendix, we review the method presented in [73].

Suppose that a density matrix ρ evolves under our simulation into $\mathcal{G}(\rho)$. The goal of QPT is to determine $\mathcal{G}$. Given a complete basis of matrices, $\tilde{E}_m$, that spans the operator space (i.e., the Liouville space), any unitary $\mathcal{G}$ can be written in the form

$$\mathcal{G}(\rho) = \sum_{m,n} \chi_{mn} \tilde{E}_m \rho \tilde{E}_n^\dagger, \tag{C1}$$

where χ_{mn} are coefficients that we wish to find. For single-qubit gates, the set $\tilde{E}_m$ contains four 2×2 matrices ($m = 1, ..., 4$) and χ_{mn} is a 4×4 matrix. Let us choose the Pauli and identity matrices as basis operators:

$$\tilde{E}_1 = I \quad , \quad \tilde{E}_2 = \sigma_x \quad , \quad \tilde{E}_3 = -i\sigma_y \quad , \quad \tilde{E}_4 = \sigma_z. \tag{C2}$$

To determine χ, we run our simulations on 4 initial states

$$\rho_1 = |0\rangle\langle 0| \ , \ \rho_2 = \rho_1 \sigma_x \ , \ \rho_3 = \sigma_x \rho_1 \ , \ \rho_4 = \sigma_x \rho_1 \sigma_x. \tag{C3}$$

We compute the final state for every input: $\rho_i' \equiv \mathcal{E}(\rho_i)$. Then, following [73], χ is given by

$$\chi = \frac{1}{4} \begin{pmatrix} I & \sigma_x \\ \sigma_x & I \end{pmatrix} \begin{pmatrix} \rho_1' & \rho_2' \\ \rho_3' & \rho_4' \end{pmatrix} \begin{pmatrix} I & \sigma_x \\ \sigma_x & I \end{pmatrix}. \tag{C4}$$

where $I, \sigma_x, \rho_1', ..., \rho_4' \in \mathbb{R}^{2\times2}$ and $\chi \in \mathbb{R}^{4\times4}$.

For two-qubit gates, we write

$$\mathcal{G}(\rho) = \sum_{m,n} \chi_{mn} \tilde{E}_m^{(2)} \rho (\tilde{E}_n^{(2)})^\dagger \tag{C5}$$

in terms of two-qubit operators, $\tilde{E}_m^{(2)} \in \mathbb{R}^{4\times4}$, defined as Kronecker products of the single-qubit basis operators, $\tilde{E}_m$, from Eq. (C2). The matrix $\chi \in \mathbb{R}^{16\times16}$ is given by

$$\chi = \Lambda\,\bar{\rho}\,\Lambda, \tag{C6}$$

where $\Lambda \in \mathbb{R}^{16\times16}$ is a rotation matrix

$$\Lambda \equiv \frac{1}{4}\left[\begin{pmatrix} I & \sigma_x \\ \sigma_x & I \end{pmatrix} \otimes \begin{pmatrix} I & \sigma_x \\ \sigma_x & I \end{pmatrix}\right] \tag{C7}$$

and $\bar{\rho} \in \mathbb{R}^{16\times16}$ is defined as

$$\bar{\rho} = P^T \rho' P. \tag{C8}$$

Here, $\rho' \in \mathbb{R}^{16\times16}$ the matrix of final states

$$\rho' = \mathcal{G}(\rho), \tag{C9}$$

found by propagating 16 input states

$$\rho_{mn} = T_n |00\rangle\langle00| T_m \quad \forall n, m = 1, ..., 4 \tag{C10}$$

with

$$\begin{aligned} T_1 &= I \otimes I \quad, \quad T_2 = I \otimes \sigma_x \\ T_3 &= \sigma_x \otimes I \quad, \quad T_4 = \sigma_x \otimes \sigma_x. \end{aligned} \tag{C11}$$

The permutation matrix P is given by

$$P = I \otimes \left[\begin{pmatrix} 1 & 0 & 0 & 0 \\ 0 & 0 & 1 & 0 \\ 0 & 1 & 0 & 0 \\ 0 & 0 & 0 & 1 \end{pmatrix} \otimes I\right]. \tag{C12}$$

Note that $I \in \mathbb{R}^{2\times2}$ and, hence, $P \in \mathbb{R}^{16\times16}$.

D   Noise Analysis

We follow the analysis of [24]. The equations that we used to simulate the various noise processes are detailed below.

I. Doppler shifts and fluctuations in atomic separation

Finite temperature effects give rise to fluctuations in atomic velocity and position. The former produce shifts in the effective single-photon detuning while the latter introduce a variation in the Rydberg interaction strength. To see how this comes about, let us write the Hamiltonian. We denote atomic positions by $\mathbf{R}_\ell(t) = \mathbf{R}_\ell + \delta\mathbf{R}_\ell + \mathbf{v}_\ell t$, where the index relates to the ℓth atom, $\delta\mathbf{R}_\ell$ are position deviations and $\mathbf{v}_\ell$ are the atomic velocities. The Hamiltonian is:

$$H = \sum_\ell \left\{ \frac{\Omega_1(t)}{2} e^{i\mathbf{k}_1 \cdot \mathbf{R}_\ell(t)} |1_\ell\rangle\langle p_\ell| + \frac{\Omega_2(t)}{2} e^{i\mathbf{k}_2 \cdot \mathbf{R}_\ell(t)} |p_\ell\rangle\langle r_\ell| + \text{h.c.} - \Delta |p_\ell\rangle\langle p_\ell| \right\} + V_R(|\mathbf{R}_1 - \mathbf{R}_2|)|r_1 r_2\rangle\langle r_1 r_2| \tag{D1}$$

where $\mathbf{k}_j$ is the wavevector of the control pulses Ω_j. We assume in our analysis that the control pulses and the tweezer beams are co-propagating along the z direction (i.e., the wavevectors are parallel). The atoms are placed along an axis perpendicular to z (say along the x direction). Using the parameters from [6], we consider a temperature of 10 μK which produces a normal distribution of detunings with standard deviation $2\pi \times 43$ kHz. Assuming tightly focused tweezer beams, we a distribution of positions with standard deviation of 200 nm.

II. Spatial dependence of the pulse amplitude

The control pulses are Gaussian beams. For simplicity, we consider the effect of amplitude fluctuations due to atom deviation from the trap center in the transverse direction (x,y) only. Hence, the amplitude of control pulse $j = 1, 2$ depends on the transverse (x,y) coordinates of atom ℓ via the relation:

$$\Omega_j(t, \mathbf{R}_\ell) = \Omega_j(t, 0) e^{(x_\ell^2 + y_\ell^2)/w^2} \tag{D2}$$

where w is the beam waist, chosen here to be $w = 1\mu\text{m}$. We generate a random distribution of locations corresponding to a temperature of 10 μK, using trap parameters from [24].

III. Noise in the amplitude and phase of the control fields

Classical noise in the amplitude of the control fields is accounted for by generating an ensemble of amplitude deviations $\Omega_j \to \Omega_j + \delta_j$ and averaging over the resulting fidelity. Previous work has shown that this noise channel has little effect on STIRAP-based protocols and we confirm this result. Laser phase noise has an average effect of introducing a dephasing channel, which is conveniently modeled by an appropriate jump term in the Lindbladian. Specifically, following [24], we include a term of the form $\sqrt{\gamma_1/2}(|p\rangle \langle p| - |1\rangle \langle 1|)$ and $\sqrt{\gamma_2/2}(|r\rangle \langle r| - |p\rangle \langle p|)$ to account for the noise in each control field.